JOURNAL OF SYNCHROTRON RADIATION

ISSN 1600-5775

Dynamical effects on superradiant THz emission from an undulator

Gianluca Geloni, Takanori Tanikawa and Sergey Tomin*

European XFEL, Hamburg, Germany. *Correspondence e-mail: sergey.tomin@xfel.eu

Received 26 October 2018
Accepted 18 February 2019

Edited by D. A. Reis, SLAC National Accelerator Laboratory, USA

Keywords: undulator radiation; superradiant emission; chirped electron bunch; dispersion.

Superradiant emission occurs when ultra-relativistic electron bunches are compressed to a duration shorter than the wavelength of the light emitted by them. In this case the different electron contributions to the emitted field sum up in phase and the output intensity scales as the square of the number of electrons in the bunch. In this work the particular case of superradiant emission from an undulator in the THz frequency range is considered. An electron bunch at the entrance of a THz undulator setup has typically an energy chirp because of the necessity to compress it in magnetic chicanes. Then, the chirped electron bunch evolves passing through a highly dispersive THz undulator with a large magnetic field amplitude, and the shape of its longitudinal phase space changes. Here the impact of this evolution on the emission of superradiant THz radiation is studied, both by means of an analytical model and by simulations.

1. Introduction

As has been well known for a long time, superradiant emission of radiation[1] from ultrarelativistic electron bunches takes place when the duration of the bunches is shorter than the radiation wavelength (Nodvick & Saxon, 1954). In this case, the contributions to the field from all electrons sum up in phase, and the output intensity scales as the square of the number of electrons in the bunch.

This description can be made mathematically precise by modelling the electric field from a given electron bunch in a fixed radiation setup with

$$\mathbf{E}(\mathbf{r}, t) = \sum_{j=1}^{N_e} \mathbf{E}_1\left(\mathbf{l}_j, \boldsymbol{\eta}_j, \gamma_j, \tau_j; \mathbf{r}, t\right), \tag{1}$$

where $\mathbf{E}_1$ is the field from a single electron, N_e is the number of electrons, and the phase space position of the jth electron at the entrance of the radiator setup is specified by $(\mathbf{l}_j, \boldsymbol{\eta}_j, \gamma_j, \tau_j)$. In particular, given the jth electron, $\mathbf{l}_j$ indicates its transverse position with respect to the z-axis, which coincides with the radiator axis, $\boldsymbol{\eta}_j$ is the angle formed by the electron trajectory with respect to z, γ_j is the electron energy in units of $m_e c^2$ (m_e being the electron rest mass, and c the speed of light in vacuum) and τ_j is the arrival time of the electron at the entrance of the radiator, which is calculated assuming that the reference electron, labelled with $j = 0$, arrives at $\tau_0 = 0$. If the electron distribution in phase space, normalized to unity, is given by

$$f(\mathbf{l}, \boldsymbol{\eta}, \gamma, \tau) = f_\tau(\tau)\, \delta(\mathbf{l})\, \delta(\boldsymbol{\eta})\, \delta(\gamma - \gamma_0), \tag{2}$$

one obtains

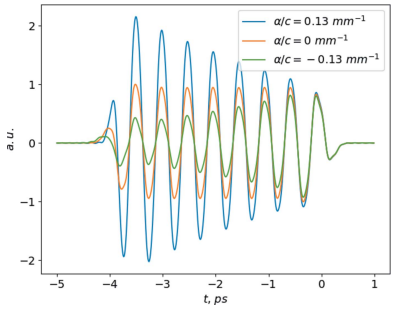

[1] Also known as coherent emission.

$$\mathbf{E}(t) = \sum_{j=1}^{N_e} \mathbf{E}_1(t - \tau_j). \tag{3}$$

If one now indicates with $\mathbf{E}(\omega)$ the Fourier transform of the electric field with respect to time and with $\widetilde{\mathbf{E}}(\omega) = \mathbf{E}(\omega)\exp(-i\omega z/c)$ the slowly varying amplitude of the field in the frequency domain, in short 'the field', one obtains

$$\widetilde{\mathbf{E}}(\omega) = \sum_{j=1}^{N_e} \widetilde{\mathbf{E}}_1(\omega)\exp(i\omega\tau_j). \tag{4}$$

By averaging the field over an ensemble of electron bunches (this operation will be indicated by angular brackets $\langle \ldots \rangle$) the ensemble-averaged intensity is found to be

$$\begin{aligned}\langle I(z, \mathbf{r}, \omega)\rangle &= \frac{c}{2\pi}\left\langle \left|\widetilde{\mathbf{E}}(z, \mathbf{r}, \omega)\right|^2 \right\rangle \\ &= \frac{c}{2\pi}\left|\widetilde{\mathbf{E}}_1(z, \mathbf{r}, \omega)\right|^2 \left[N_e + N_e(N_e - 1)\left|\bar{f}_\tau(\omega)\right|^2\right],\end{aligned} \tag{5}$$

where

$$\bar{f}_\tau(\omega) = \int \mathrm{d}\tau\, f_\tau(\tau)\exp(i\omega\tau). \tag{6}$$

Note that the corresponding power can be found by integrating equation (5) in d^2r over the transverse plane.

This is a well known expression [see, for example, Williams (2004) and references therein] that models incoherent [the first term in equation (5)] and coherent [the second term in equation (5)] emission, whenever a cold, zero-emittance electron beam with finite duration and given temporal profile f_τ is considered.

In this article we generalize equation (5) accounting for the phase space distribution

$$f(\mathbf{l}, \boldsymbol{\eta}, \gamma, \tau) = f_\tau(\tau)\,\delta(\mathbf{l})\,\delta(\boldsymbol{\eta})\,\delta\big[\gamma - (\gamma_0 + \alpha\tau)\big], \tag{7}$$

normalized to unity, which still models a cold beam without uncorrelated energy spread, but accounts for an energy chirp along the bunch through the constant α, which has the dimension of inverse time, and can assume both positive or negative values and indicates the slope of the chirp. We will focus on the particular case of superradiant emission of radiation from an electron bunch with this kind of phase-space distribution passing through an undulator. Aside for theoretical interest [a semi-analytical expression generalizing equation (5) is not known, at least to the authors' knowledge], there is an important practical reason for this study, which is its relevance to the case of superradiant, undulator-based THz sources of radiation (Gensch *et al.*, 2008; Green *et al.*, 2016; Tanikawa *et al.*, 2018), for which there is a need for modelling and understanding, from a theoretical viewpoint, the shape of the emitted waveform that can be directly measured in the time domain with electro-optical techniques (see Fig. 1).

While an analysis of experimental data in the time-domain is left to future work, in this paper we provide theoretical tools that can be applied to perform such an analysis (see the time-domain study in §3.2.6).

In particular, we include in our considerations an important effect that has not been considered up to now, which is due

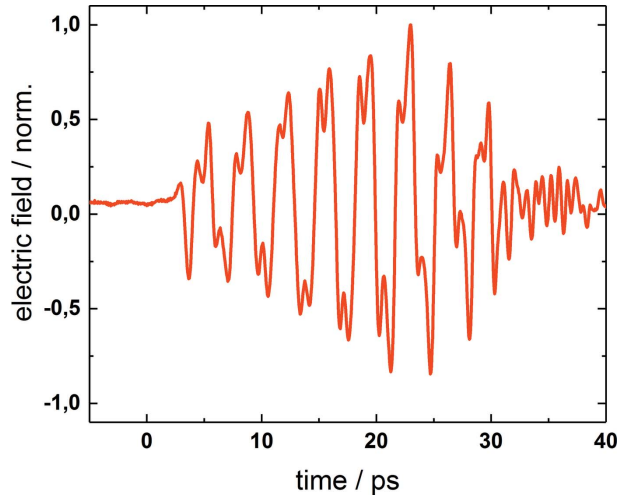

Figure 1
THz electric field as determined for an undulator tuned to 0.27 THz at the superradiant THz user facility TELBE (Green *et al.*, 2016). Courtesy of M. Gensch, HZDR.

to the fact that an electron bunch at the entrance of a THz undulator setup has typically an energy chirp that can be approximatively described as in equation (7). Suppose that electrons with smaller energy are at the head of the bunch, *i.e.* $\alpha > 0$. When such an electron bunch travels along the undulator, due to dispersion, the electron beam will tend to shrink. Now, near resonance we know that electrons are overtaken by radiation of a wavelength every undulator period, and usually the before-mentioned effect is small. However, for long wavelength in the millimetre range, dispersion effects become non-negligible, and one can potentially control the duration of the electron bunch, and hence the wavelength reach of superradiant emission, by imposing an initial chirp on the electron beam. A chirp of opposite sign would, of course, result in the opposite effect. In this paper we lay the foundation for these kinds of manipulations.

In Section 2 we present analytical calculations. In Section 3 we present the results from our semi-analytical model, and we compare them with the output of simulation codes, showing that, indeed, the effect of an energy chirp on the superradiant emission can be non-negligible. Finally, in Section 4 we present our conclusions.

2. Analytical model

We consider an electron beam phase space described by equation (7). Note that in this case a realization of the electric field distribution in time and frequency domains are

$$\mathbf{E}(\mathbf{r}, t) = \sum_{j=1}^{N_e} \mathbf{E}_1(\gamma_0 + \alpha\tau_j; \mathbf{r}, t - \tau_j) \tag{8}$$

and[2]

[2] As before, we will refer to the slowly varying envelope of the Fourier transform of the electric field.

$$\widetilde{\mathbf{E}}(z,\theta,\omega)=\sum_{j=1}^{N_e}\widetilde{\mathbf{E}}_1\left(\gamma_0+\alpha\tau_j;z,\theta,\omega\right)\exp\left(i\omega\tau_j\right). \quad (9)$$

We will only consider the case of planar undulator radiation at resonance, and we underline the fact that the phase space position refers to the entrance of the undulator. This remark is important, because the phase space distribution evolves as the electron beam moves along the undulator axis z.

In particular we should consider that the kth electron arrives at time $t=\tau_k$, with respect to the reference electron (arriving at $t=0$), so that values of $\tau_k>0$ indicate a delay, while $\tau_k<0$ indicates an advance of the kth electron *at the entrance of the undulator*. Then, we can calculate the slippage after a distance $\delta z'=z_2-z_1$ has been travelled along the undulator as

$$c\left[\frac{s(z_2)-s(z_1)}{v}-\frac{z_2-z_1}{c}\right]=\int_{z_1}^{z_2}\mathrm{d}\bar{z}\,\frac{1}{2\gamma_z^2(\bar{z})}=\frac{\delta z'}{\lambda_w}\lambda_{1k}$$
$$=\frac{\delta z'(1+K^2/2)}{2(\gamma_0+\alpha\tau_k)^2}. \quad (10)$$

Here $s(z)$ is the curvilinear abscissa at position z, v is the electron speed, γ_z is the longitudinal Lorentz factor, λ_w the undulator period, λ_{1k} the undulator fundamental wavelength for the kth electron and K the undulator parameter. The difference between the value of the slippage for the kth particle with $\gamma=\gamma_0+\alpha\tau_k$ and for the reference with $\gamma=\gamma_0$ is

$$\Delta s(\delta z')=\frac{\delta z'(1+K^2/2)}{2(\gamma_0+\alpha\tau_k)^2}-\frac{\delta z'(1+K^2/2)}{2\gamma_0^2}$$
$$\simeq-\frac{\delta z'(1+K^2/2)}{\gamma_0^3}\,\alpha\tau_k. \quad (11)$$

It follows that

$$R_{56}(\delta z')=-\frac{\delta z'(1+K^2/2)}{\gamma_0^2}, \quad (12)$$

with the fractional energy deviation from γ_0 being given by $\Delta\gamma/\gamma_0=\alpha\tau_k/\gamma_0$ and $\Delta s(\delta z')=R_{56}(\delta z')\Delta\gamma/\gamma_0$. Here we remind that R_{56} is related to the momentum compaction, and is an element of the transfer matrix of the setup.[3]

This means that, if the kth electron arrives at time τ_k at the entrance of the undulator, then in the middle of the undulator the arrival time will be changed to $\tau_k[1+R_{56}(L_u/2)\alpha/(\gamma_0 c)]$.

Now, for the reference electron, the undulator radiation around resonance in the far-zone is [see, among many others, Onuki & Elleaume (2003)]

$$\widetilde{\mathbf{E}}_1(z,\theta,\omega)=-\frac{K\omega e L_u A_{JJ}}{2\gamma_0 c^2 z}\exp\left[i\frac{\omega\theta^2 z}{2c}\right]$$
$$\times\,\mathrm{sinc}\left[\frac{L_u}{2}\left(C+\frac{\omega\theta^2}{2c}\right)\right]\hat{e}_y, \quad (13)$$

where

$$C=\frac{\omega}{2\bar{\gamma}_{0z}^2 c}-k_u=\frac{\Delta\omega}{\omega_1}k_u \quad (14)$$

is the detuning from resonance, with $\Delta\omega=\omega-\omega_{10}$,

$$\bar{\gamma}_{0z}=\frac{\gamma_0}{(1+K^2/2)^{1/2}}, \quad (15)$$

while $A_{JJ}\equiv J_1(u)-J_0(u)$, and $u=K^2\omega/(8\gamma^2 k_u c)$, and around resonance $\omega_{10}=2k_u c\bar{\gamma}_{0z}^2$ we have $u\simeq K^2/[2(2+K^2)]$.

Then, dropping the vector notation, the field from the reference electron can also be written as

$$\widetilde{E}_1=-\frac{K\omega e A_{JJ}}{2\gamma_0 c^2 z}\exp\left[i\frac{\omega\theta^2 z}{2c}\right]$$
$$\times\int_{-L_u/2}^{L_u/2}\mathrm{d}z'\exp\left[i\left(\frac{\omega\theta^2}{2c}+\frac{\omega-\omega_{10}}{\omega_{10}}k_u\right)z'\right]. \quad (16)$$

In order to obtain the total field we need to find the field from the kth electron and sum over all electrons. This can be done by remembering that γ_0 has to be replaced by $\gamma_k=\gamma_0+\alpha\tau_k$ in all instances in equation (16), including the resonance frequency that is now $\omega_{1k}=2k_u c\bar{\gamma}_{kz}^2$ instead of ω_{10} and that, in the middle of the undulator, the arrival time of the kth electron is given by $\tau_k[1+R_{56}(L_u/2)\alpha/(\gamma_0 c)]$, with R_{56} as in equation (12),

$$\widetilde{E}=-\sum_{k=1}^{N_e}\frac{K\omega e A_{JJ}}{2(\gamma+\alpha\tau_k)c^2 z}\exp\left[i\frac{\omega\theta^2 z}{2c}\right]$$
$$\times\int_{-L_u/2}^{L_u/2}\mathrm{d}z'\exp\left[i\left(\frac{\omega\theta^2}{2c}+\frac{\omega-\omega_{1k}}{\omega_{1k}}k_u\right)z'\right]$$
$$\times\exp\left\{i\omega\tau_k\left[1-\frac{L_u(1+K^2/2)\alpha}{2\gamma_0^3 c}\right]\right\}. \quad (17)$$

Equation (17) can also be rewritten as

$$\widetilde{E}(z,\theta,\omega)=-\frac{K\omega e A_{JJ}}{2c^2 z}\exp\left[i\frac{\omega\theta^2 z}{2c}\right]$$
$$\times\int_{-L_u/2}^{L_u/2}\mathrm{d}z'\exp\left[i\left(\frac{\omega\theta^2}{2c}-k_u\right)z'\right]$$
$$\times\sum_{k=1}^{N_e}\frac{1}{(\gamma_0+\alpha\tau_k)}\exp\left\{\frac{i\omega(1+K^2/2)\,z'}{2c(\gamma_0+\alpha\tau_k)^2}\right.$$
$$\left.+i\omega\tau_k\left[1-\frac{L_u(1+K^2/2)\,\alpha}{2\gamma_0^3 c}\right]\right\}. \quad (18)$$

We now perform the following two approximations:

(i) We approximate $\gamma_0+\alpha\tau_k\simeq\gamma_0$ in the denominator of equation (18).

(ii) We expand the phase factor in γ_k in equation (18) to the first order in α, that is we assume

$$\frac{i\omega(1+K^2/2)z'}{2c(\gamma_0+\alpha\tau_k)^2}\simeq\frac{i\omega(1+K^2/2)z'}{2c\gamma_0^2}-\frac{i\omega(1+K^2/2)z'}{c\gamma_0^3}\alpha\tau_k. \quad (19)$$

[3] The transfer matrix transforms the electron phase-space at two different positions along the undulator, in our case the undulator entrance and $\delta z'$.

Both assumptions are verified for all electrons when $\alpha\sigma_\tau/\gamma_0 \ll 1$ and $3(\alpha\sigma_\tau)^2 k_u L_u/\gamma_0^2 \ll 1$. These conditions need to be verified case by case for the theory to be valid.

Substitution into equation (18) gives

$$\widetilde{E}(z,\theta,\omega) = -\frac{K\omega e A_{JJ}}{2c^2\gamma_0 z}\exp\left[i\frac{\omega\theta^2 z}{2c}\right] \times \int_{-L_u/2}^{L_u/2} dz' \exp\left[i\left(\frac{\omega\theta^2}{2c}+\frac{\omega-\omega_{10}}{\omega_{10}}k_u\right)z'\right] \times \sum_{k=1}^{N_e}\exp\left\{i\omega\left[1-\frac{1+K^2/2}{c\gamma_0^3}\alpha(z'+L_u/2)\right]\tau_k\right\}, \quad (20)$$

where we remind that ω_{10} is the resonance frequency for the reference electron with $\gamma = \gamma_0$. We now calculate the ensemble-averaged intensity to find the following generalization of the usual formula for coherent and incoherent emission (a detailed derivation can be found in Appendix *A*),

$$\langle I(z,\theta,\omega)\rangle = N_e\frac{K^2\omega^2e^2A_{JJ}^2}{8\pi c^3\gamma_0^2}\left\{\int_0^\infty d\gamma\, f_\gamma(\gamma) \times\left|\int_{-L_u/2}^{L_u/2} dz' \exp\left[i\left(\frac{\omega\theta^2}{2c}+\frac{\omega-2k_uc\bar{\gamma}_z^2}{2c\bar{\gamma}_z^2}\right)z'\right]\right|^2 + (N_e-1)\left|\int_{-L_u/2}^{L_u/2} dz' \times \exp\left[i\left(\frac{\omega\theta^2}{2c}+\frac{\omega-\omega_{10}}{\omega_{10}}k_u\right)z'\right] \times \bar{f}_\tau\left[\omega\left(1-\frac{1+K^2/2}{c\gamma_0^3}\alpha(z'+L_u/2)\right)\right]\right|^2\right\}, \quad (21)$$

where $f_\gamma(\gamma) = \int d\tau\, d^2\eta\, d^2l\, f(\mathbf{l},\boldsymbol{\eta},\gamma,\tau)$.

Equation (21) generalizes equation (5) and in fact reduces to it for $\alpha = 0$. The first term is the incoherent radiation contribution $\langle I_{inc}\rangle \simeq N_e$, while the second term $\langle I_{coh}\rangle \simeq N_e(N_e-1)$ describes the coherent, or superradiant emission.

The coherent part of equation (21) automatically includes a change in the relative positions of electrons due to dispersion in the undulator. This dispersion leads to the phase factor depending on α in equation (20). This factor is then included in $\bar{f}_\tau$, so that the form factor evolves along the undulator as a function of z': the factor inside the round parenthesis in the argument of $\bar{f}_\tau$ [see equation (21)] shrinks or expands the reach in frequencies for coherent emission. When $z' = -L_u/2$, *i.e.* at the entrance of the undulator, this multiplication factor is just equal to unity, resulting in the usual form factor $\bar{f}_\tau(\omega)$.

Moving inside the undulator, depending on the sign of α, *i.e.* on the slope of the energy correlation, we have a modification of the form factor instead. Note that this modification takes place in general, not only for undulator radiation at resonance. A more detailed discussion can be found in Appendix *B*.

3. Comparison between analytical model and simulations: a simple case study

In this section we compare the results from our analytical model with numerical simulations. In fact, the analytical model is based on the resonance approximation, while usually THz undulator setups consist of a small number of periods. Differences are, therefore, to be expected when a realistic case is considered. The analytical approach is nevertheless still useful for a better physical understanding, for quick estimations, and for cross-checking numerical calculations in the limit for a large number of undulator periods. This last step was actually the first to be taken during our simulation studies. From a methodological point of view, we proceeded with our simulations in two steps: first, we considered the influence of the chirp from a beam dynamics standpoint and, second, we calculated radiation from the chirped beam. This is correct as long as no self-effects are impacting on the electron beam. We verified this fact separately, using the *OCELOT* toolkit (Agapov *et al.*, 2014), which was exploited for nearly all the simulations in this paper.

3.1. Choice of simulation parameters

The presence of energy chirp in the electron beam is typical and is a consequence of the bunch compression technique used[4], which we assume based on magnetic compression, as is often the case for THz light sources based on a linear accelerator like TELBE (Green *et al.*, 2016) or the FLASH THz undulator (Gensch *et al.*, 2008) just to name two.

From a beam dynamics point of view, as already discussed, it is the energy chirp – in conjunction with a large R_{56} due to the long fundamental wavelength – that leads to cases when the additional beam compression or decompression might not be negligible.

Here we choose a coordinate system with $\zeta = c\tau$ so the beam head is on the left side of graphs. Then, the beam energy chirp can be negative (in the case of over-compression) or positive, and it can vary over a wide range: in extreme cases (see, for example, Zagorodnov *et al.*, 2016) for a study dedicated to the European XFEL, the energy gradient over the bunch length in an over-compression scenario can be $E' = dE/d\zeta \simeq -1000\ \mathrm{MeV\ mm^{-1}}$ at 14 GeV and in combination with a corrugated structure $E' \simeq -5000\ \mathrm{MeV\ mm^{-1}}$. In order to choose realistic simulation parameters we limited ourself to the case of FLASH (FLASH, 2018; Ackermann *et al.*, 2007; Gensch *et al.*, 2008). The main FLASH accelerator and THz undulator parameters are listed in Table 1.

We further specialize our discussion to the case of a 500 pC, 1 GeV electron beam, as simulated in DESY S2E Simulations (2013), at the entrance of the FLASH1 VUV undulator; see the longitudinal beam phase space distribution and beam current in Fig. 2. For the sake of simplicity, we assume that the electron beam does not evolve during the passage through the FEL undulator: in other words, we do not model the effects of

[4] Here we are not considering self-effects (*e.g.* wakefields, coherent synchrotron radiation), which can further influence the energy chirp.

Table 1
The main FLASH accelerator parameters (FLASH, 2018; Ackermann *et al.*, 2007; Gensch *et al.*, 2008).

Accelerator	
Electron beam energy	0.35–1.25 GeV
Electron bunch charge	0.1–1.2 nC
Peak current	1–2.5 kA
Undulator	
Type	Planar electromagnetic undulator
Period	400 mm
Number of periods	9
K-value	3–49
Output THz radiation	
Wavelength	10–230 µm
Photon energy	5–125 meV
Photon frequency	1.3–30 THz
Photon pulse energy (average)	10–100 µJ

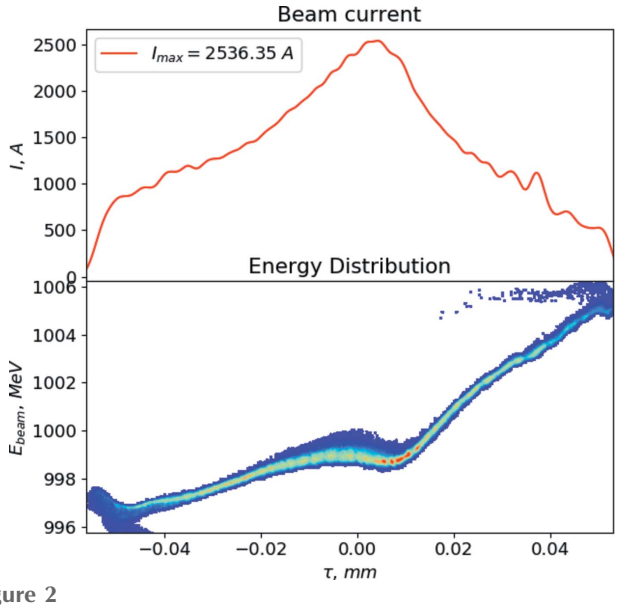

Figure 2
Beam current and energy distribution from start-to-end simulations for FLASH, according to the data reported in DESY S2E Simulations (2013).

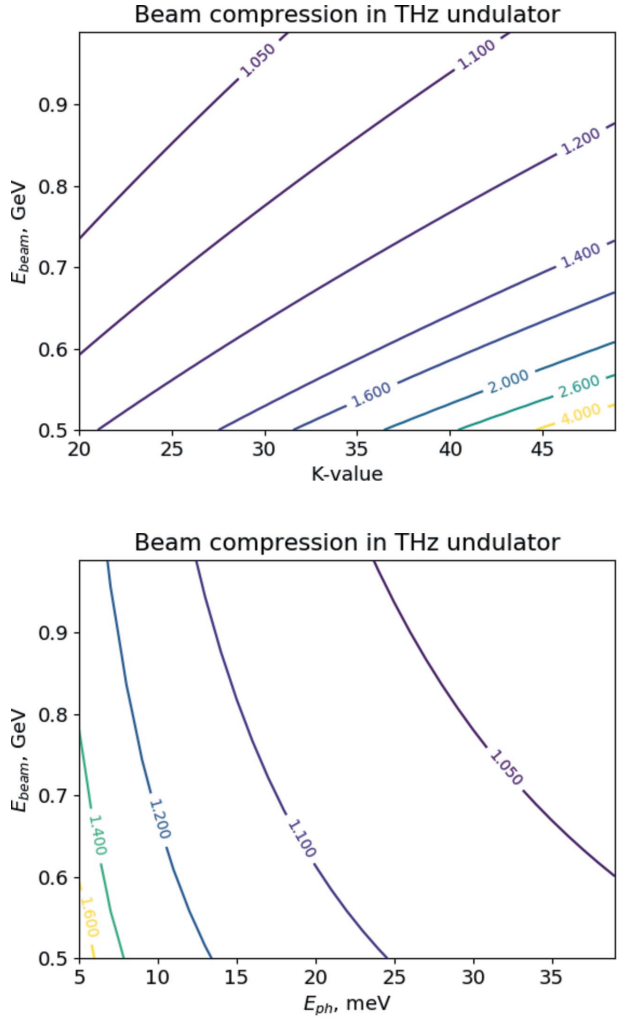

Figure 3
Compression function C for the FLASH1 THz undulator as function of beam energy and undulator K parameter (top) or, alternatively, as a function of beam energy and photon energy $E_{\rm ph}$ (bottom).

the FEL process on the electron beam. Space charge as well as resistive wakefield effects due to the vacuum chamber are assumed to be small. We then picked our energy chirp to be, in agreement with Fig. 2, $E' = 80$ MeV mm^{-1}.

The compression function $\widetilde{C} = (\partial s_f/\partial s_i)^{-1}$, which quantifies the compression for the particles in the neighbourhood of position s_i (that is the position in the bunch before the undulator) can be explicitly written as [for example, see Zagorodnov & Dohlus (2011)]

$$\widetilde{C} = \left(1 - R_{56}\,\frac{\alpha}{c}\right)^{-1} = \left(1 - \frac{1 + K^2/2}{\gamma^2}\,\frac{\alpha}{c}\,L_{\rm u}\right)^{-1}, \qquad (22)$$

where $\alpha = c\delta' = cE'/E_0$ is the energy chirp parameter defined earlier, while R_{56} pertains to the undulator and is defined in equation (12). Since at FLASH there are accelerator modules after the last bunch compressor, the final energy of the electron beam can be varied from 450 MeV to 1200 MeV without changing the compression scenario, and accordingly the beam energy gradient remains the same. Therefore, the energy chirp is inversely proportional to the electron beam energy: $\alpha(E) = cE'/E$. Taking all of this into account, we can calculate the compression function in terms of two variables: the undulator K parameter and the electron beam energy $E_{\rm beam}$, see Fig. 3(*a*), or alternatively the photon energy $E_{\rm ph}$ and the electron beam energy $E_{\rm beam}$, see Fig. 3(*b*).

As one can see from Fig. 3, the compression function takes values up to 1.4 and more for low electron beam energies (lower than 700 MeV) and large K-values (larger than 30), which correspond to low energetic radiation with photon energies lower than 10 meV, *i.e.* in our region of interest.

It is also worth mentioning that for cases with a larger energy chirp, the region in the parametric plots in Fig. 3 corresponding to large compression factors widens up.

Summarizing our previous discussion, we report the full list of our simulation parameters in Table 2.

Table 2
Simulation parameters.

Electron beam	
Electron beam energy	0.6 GeV
Electron bunch charge	0.5 nC
Peak current	1.45 kA
Transverse phase space: $\sigma_{x,y,x',y'}$	0
Energy spread, σ_E	0
Longitudinal size, σ_ζ	43 µm
Energy gradient, E'	80 MeV mm^{-1}
Energy chirp, α/c	0.13/−0.13/0
Number of macroparticles	30000
Undulator	
Period	400 mm
Number of periods	9
Amplitude of magnetic field	1.2 T
K-value	44.821
R_{56} at 600 MeV	−2.63 mm
Compression factor $\tilde{C}$	1.52/0.74/1
Output THz radiation	
Wavelength	145.8 µm
Photon energy	8.5 meV
Frequency	2.05 THz

3.2. Simulation results

Using simulation parameters from Table 2 we generated three beam distributions: one with zero energy chirp and two with opposite energy chirp signs (see also the following subsections). While the average beam energy for all three cases is the same, 600 MeV, the effect of different energy chirps on electron beam dynamics and radiation output will vary. In the case of positive energy chirp ($\alpha > 0$) we expect a growing current (because of beam shortening) and a higher contribution to radiation around the fundamental harmonics. In the case of negative energy chirp ($\alpha < 0$) the effect will be opposite. Finally, for the case of no chirp ($\alpha = 0$) the beam will be unchanged during the evolution through the undulator.

Note that in the analytical approach we used a 'cold' beam approximation and we assumed zero transverse emittance, this last assumption being justified by the long radiation wavelength, compared with the geometrical emittance of an XFEL-class beam. Therefore, we generated a zero-emittance, zero-energy-spread beam with Gaussian distribution in the longitudinal direction.

In order to simulate radiation emission we used the *OCELOT* toolkit (Agapov *et al.*, 2014), which includes a module, developed in-house, for spontaneous radiation calculations. Simulations were run in parallel on a cluster for 30000 macroparticles, which was sufficient for obtaining converging results.

We are interested in intensities as in equations (21) or (5), which are special cases of a field correlation function calculated at the same frequency and angular position. This field correlation function actually includes an ensemble average over electron bunch realizations, the stochastic process being the electron shot noise. However, here we are only interested in the calculation of the coherent part of the intensity, *i.e.* the second term in equation (21), and the radiation wavelength we are interested in is actually much longer than the longitudinal average separation between two macroparticles. As a result, for our purposes, the electron bunch distribution obtained after the macroparticle generation process is smooth, and no random process actually enters our calculations. Again, this is justified by our interest in the coherent part of the intensity, and by the fact that the distance between macroparticles is much smaller than the radiation wavelength. Then, one can simply calculate the independent radiation-field contributions from each macroparticle and sum them up taking into account the relative phases, remembering that the initial phase of the field from each macroparticle depends on its position inside the bunch,

$$\phi_j = \frac{2\pi\zeta_j}{\lambda}, \tag{23}$$

where $\zeta_j = c\tau_j$ is the longitudinal position of the macroparticle in the bunch, and λ is, as before, the wavelength of the radiation. By summing up the individual particle contributions, one obtains a total field that is independent of the macroparticles realization. Then, the coherent intensity can be calculated from the field.

3.2.1. Code validation. We first validated the code by comparing it against analytical calculations in the limit for a large number of undulator periods and in the far zone. The reason for doing this is that, as discussed before, the analytical calculations are derived under the resonance approximation and in the far zone. Obviously, as one increases the number of undulator periods, one also increases the effect of the energy chirp, because R_{56} increases. Therefore, we first performed calculations by increasing the number of undulator periods by a factor of ten (for a total of 90 periods), and by decreasing accordingly by the same factor the energy gradient to E' = 8 MeV mm^{-1} or the energy chirp α/c = 0.013 mm^{-1}. Fig. 4 shows the case for a positive chirp (top left plot). As expected, the current increases as the electron bunch travels through the undulator (top right plot). The numerically calculated radiation profile at the nominal resonant photon energy $E_{\rm ph}$ = 8.5 meV (bottom left plot) and on-axis spectrum (bottom right plot) agree with the respective analytical calculations. Small differences are to be ascribed to the accuracy of the resonance approximation. Note that in simulations we introduce the ending poles sequence (1/4, −3/4, 1, . . . , −1, 3/4, −1/4), indicating that the undulator end-poles are characterized by one-quarter and three-quarters of the on-axis magnetic field of the other poles.

After obtaining the good agreement shown in Fig. 4 (bottom plots) between analytical calculations and *OCELOT*, we moved further to consider our case study with a small number of undulator periods N_w = 9 and the parameters in Table 2.

3.2.2. Zero energy chirp. We started simulating superradiant radiation from an electron beam with zero chirp. In this case, we could perform a further cross-check with the well known code *SPECTRA* (Tanaka & Kitamura, 2001). Fig. 5 shows our results.

Note that the current profile remains the same before and after the undulator, as it should be. The very good agreement

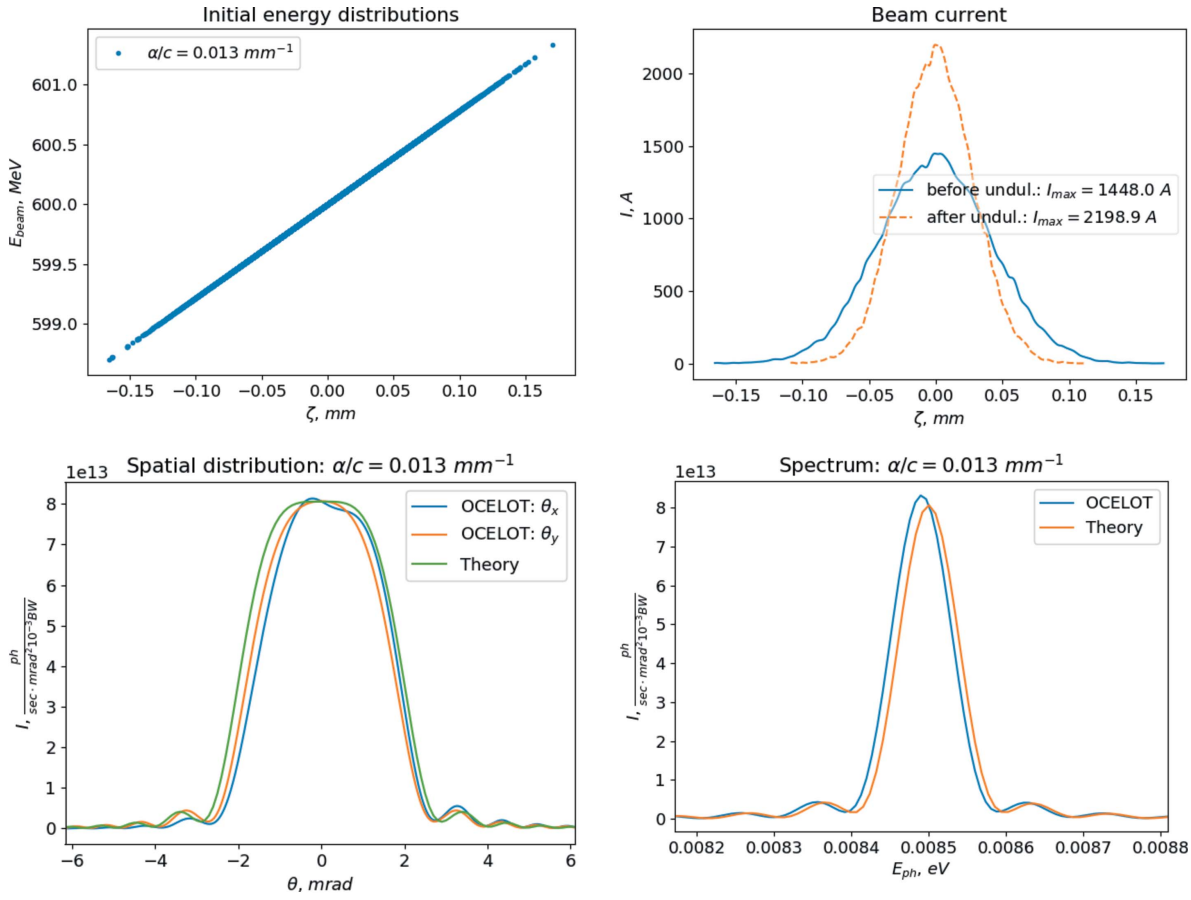

Figure 4
Energy distribution, beam current in front of and after the undulator, on-axis spectrum and far-zone spatial distribution at $E_{\rm ph}$ = 8.5 meV for beam with an increased number of undulator periods, N_w = 90, and a positive, reduced energy chirp.

between *SPECTRA* and *OCELOT* further validates our numerical simulations. As concerns the difference with respect to analytical calculations here we stress that, as was also discussed above, the resonance approximation does not hold with good accuracy for a small number of undulator periods, and differences between analytical and numerical approach are not surprising. This does not mean that the output from an actual setup will necessarily be closer to these particular numerical calculations than to the analytical ones. In fact, numerical calculations made here only assume a typical end-pole configuration to give zero first and second field integrals, but do not account for what precedes and follows the undulator, which is important if one goes beyond the resonance approximation. In other words, we underline the limited accuracy of the resonance approximation, but also the need to specify the full THz setup in order to obtain realistic simulations of the output.

3.2.3. Positive energy chirp. We performed the same simulations for a positive chirp α/c = 0.13 mm^{-1}, Fig. 6. It is interesting to note that the current amplitude is increased in accordance with the compression factor $\widetilde{C}$ = 1.5. Likewise, the output spectrum and intensity are increased by a factor of 2.6 with respect to the case of zero energy chirp.

3.2.4. Negative energy chirp. Finally, the same calculations were performed for a negative energy chirp α = −0.13 mm^{-1}, Fig. 7. This time, the beam current decreases, consistently with a compression factor $\widetilde{C}$ = 0.74, smaller than unity. Likewise, the output spectrum and intensity are decreased by a factor of 2.7 with respect to the case of zero energy chirp.

3.2.5. Maximum intensity as a function of photon energy. It is interesting to compare the maximum intensity as a function of the fundamental tune for the different chirps considered above, both for the analytical treatment and for the numerical calculations. As can be seen from Fig. 8, for positive chirps the maximum intensity is higher, and shifted towards shorter wavelengths. The difference with the analytical approximation depends once more on what preceded and what follows the undulator. In the case of Fig. 8 the undulator end-poles are, as discussed above, characterized by the sequence (1/4, −3/4, 1, . . . , −1, 3/4, −1/4), which reduces the effective number of undulator periods. If one imposes (non-physically) a cos-like undulator magnetic field profile, one obtains the result in Fig. 9.

3.2.6. Time domain analysis. The simulation results shown up to now pertain to the coherent part of the intensity in the frequency domain. In order to obtain them, we actually calculated the coherent part of the electric field in the frequency domain, whose knowledge straightforwardly allows to synthesize the field in the time domain too, via discrete inverse Fourier transform. In Fig. 10 we show field traces of

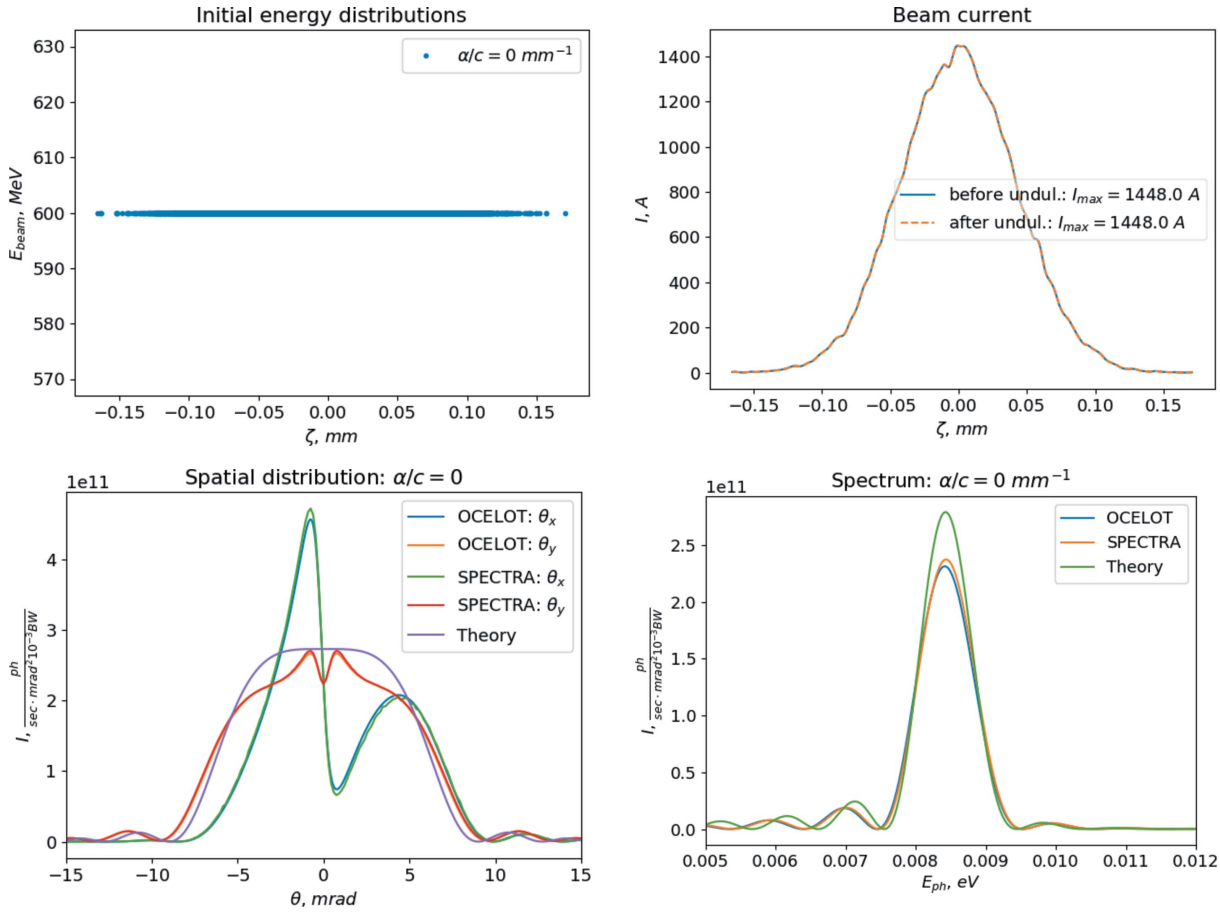

Figure 5
Energy distribution, beam current in front of and after the undulator, on-axis spectrum and far-zone spatial distribution at $E_{ph} = 8.5$ meV for a beam with no energy chirp.

the on-axis field for different chirps, obtained by synthesizing, from our previous results, photon energies between 0.1 meV and 30 meV. Since the fundamental harmonic is at 8.5 meV the traces include contributions at the first and at the third harmonics[5]. However, for the particular parameter set chosen in our simulations, see Table 2 and Fig. 11, the modulus of the form factor at the third harmonic is too small to play any role, even after compression has taken place.

The results in Fig. 10 can be easily interpreted. First of all, they refer to a large observation distance from the undulator centre, compared with the undulator length. Therefore, when there is no chirp (orange line), all poles contribute in the same way, *i.e.* the field amplitude does not depend on the position inside the pulse. When α is positive (blue line) the bunch duration shrinks along the undulator, *i.e.* the modulus of the form factor at the fundamental increases, and one observes an increase of the field amplitude along the undulator. Viceversa, when α is negative (green line) the bunch duration increases along the undulator, *i.e.* the modulus of the form factor at the fundamental decreases, and one observes a decrease of the field amplitude along the undulator.

[5] On-axis, the contribution of the even harmonics is simply zero.

While we stress once more that the present work is of pure theoretical nature, we also underline that our time-domain analysis enables a detailed study of experimentally measured data like those in Fig. 1.

4. Conclusions

This paper reports on the influence of energy chirp in the electron beam on the output from dedicated THz undulators, due to the large dispersion associated with the long fundamental wavelengths. The combination of chirp and dispersion leads to a change in the electron beam form factor as the beam goes through the undulator, and hence a modification of the superradiant output radiation. We showed both theoretically and by means of simulations that for parameters compatible with existing accelerator-based THz undulators one can expect a large deviation of the output characteristics of the THz beam compared with the usual estimations in equation (5). We discussed an analytical generalization of equation (5) for the case of undulator radiation, equation (21), which is still based on the resonance approximation and accounts for the evolution of the electron beam phase space along the undulator. We used this analytical model to validate our software tool, based on the *OCELOT* package, which

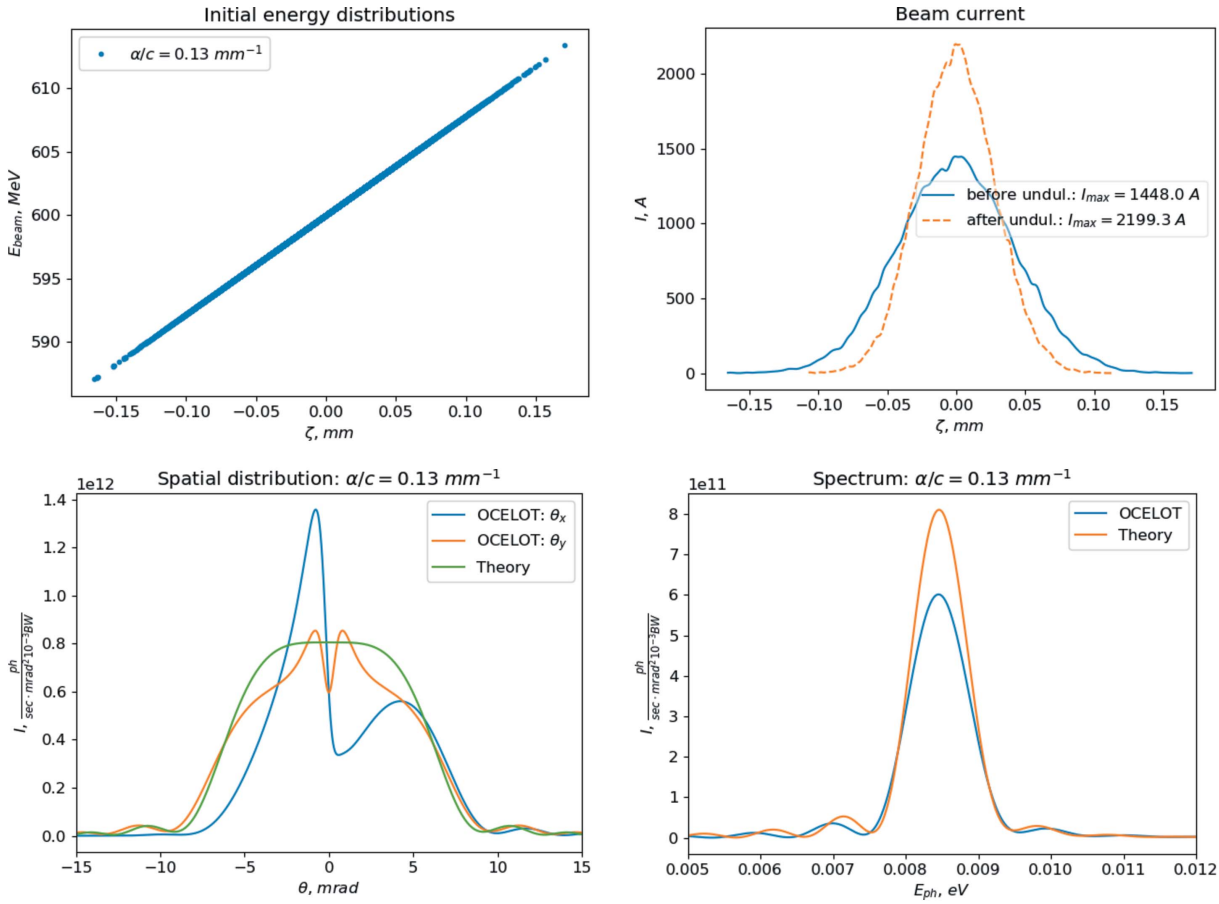

Figure 6
Energy distribution, beam current in front of and after the undulator, on-axis spectrum and far-zone spatial distribution at $E_{\rm ph}$ = 8.5 meV for beam with positive energy chirp. Calculations refer to the parameters in Table 2.

allows for both beam dynamics calculations and radiation emission calculations. Further cross-checking was performed with the help of the *SPECTRA* code. We argue that our work may be used in order to explain, at least partially, possible deviations of THz emission from the nominal expectations, calculated under the assumption that the form factor does not change as the electron beam evolves through the undulator.

APPENDIX *A*
A detailed derivation of equation (21)

We start from equation (20), which we rewrite as

$$\widetilde{E}(z,\theta,\omega) = A(z,\theta,\omega)\int_{-L_{\rm u}/2}^{L_{\rm u}/2} {\rm d}z'\, B(z',\theta,\omega) \times \sum_{j=1}^{N_{\rm e}} \exp\left[i\omega\chi(z')\tau_j\right], \tag{24}$$

with the auxiliary definitions

$$A(z,\theta,\omega) = -\frac{K\omega e A_{JJ}}{2c^2\gamma_0 z}\exp\left[i\,\frac{\omega\theta^2 z}{2c}\right], \tag{25}$$

$$B(z',\theta,\omega) = \exp\left[i\left(\frac{\omega\theta^2}{2c} + \frac{\omega-\omega_1}{\omega_1}k_{\rm u}\right)z'\right] \tag{26}$$

and

$$\chi(z') = 1 - \frac{1+K^2/2}{c\gamma_0^3}\,\alpha(z'+L_{\rm u}/2). \tag{27}$$

We use equation (24) to calculate

$$\left\langle I(z,\theta,\omega)\right\rangle = \frac{cz^2}{2\pi}\left\langle\left|\widetilde{E}\right|^2\right\rangle = \frac{cz^2}{2\pi}|A|^2\left\langle \int_{-L_{\rm u}/2}^{L_{\rm u}/2}{\rm d}z' B(z') \times \sum_{m=1}^{N_{\rm e}}\exp\left[i\omega\chi(z')\tau_m\right]\int_{-L_{\rm u}/2}^{L_{\rm u}/2}{\rm d}z'' \times B^*(z'')\sum_{n=1}^{N_{\rm e}}\exp\left[-i\omega\chi(z'')\tau_n\right]\right\rangle, \tag{28}$$

where we understood some of the variable dependencies, explicitly defined in equations (25), (26) and (27).

We now remember that in general

$$f_\tau(t) = \frac{1}{N_{\rm e}}\left\langle\sum_{j=1}^{N_{\rm e}}\delta(t-\tau_j)\right\rangle \tag{29}$$

and

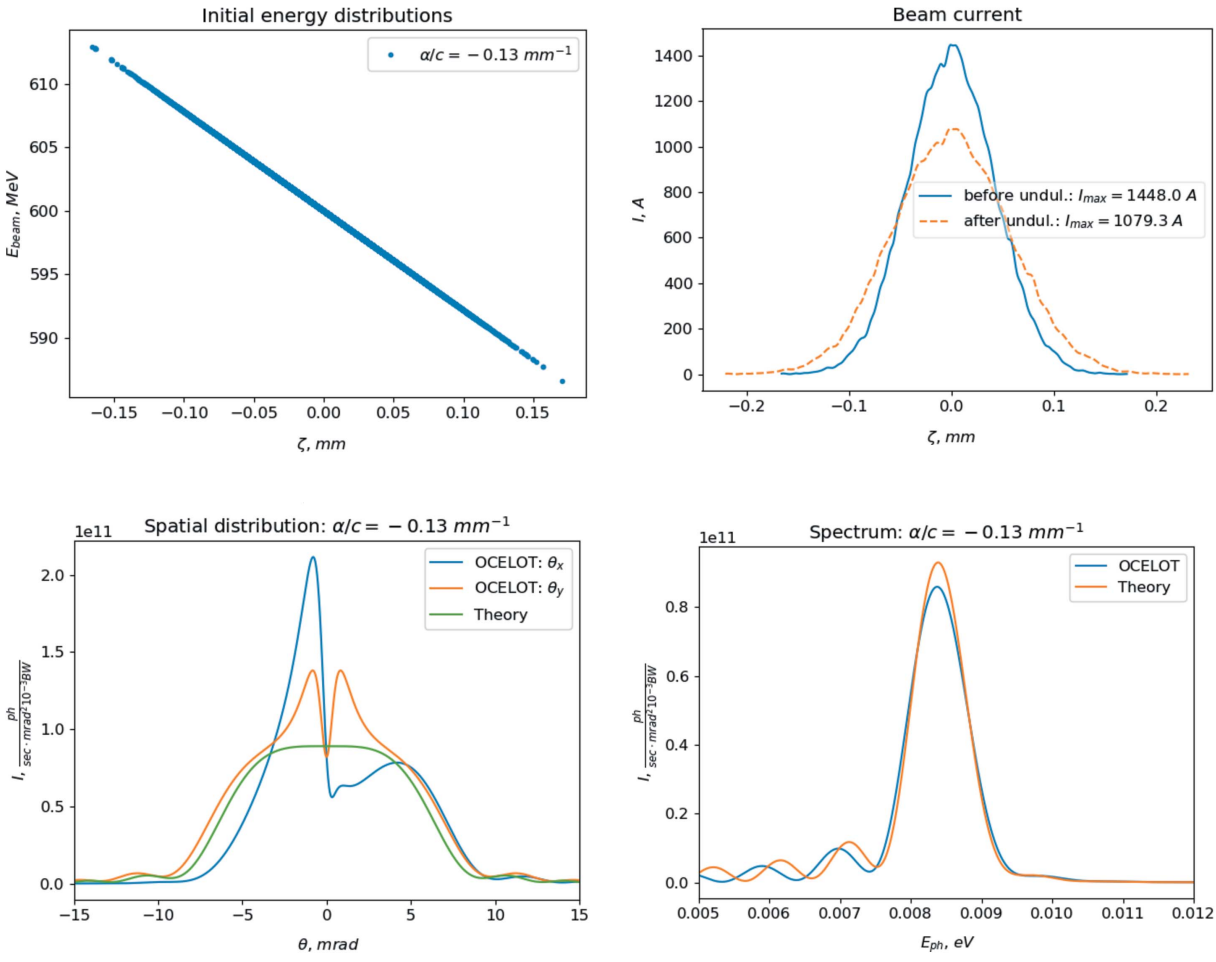

Figure 7
Energy distribution, beam current in front of and after the undulator, on-axis spectrum and far-zone spatial distribution at $E_{ph} = 8.5$ meV for beam with negative energy chirp. Calculations refer to the parameters in Table 2.

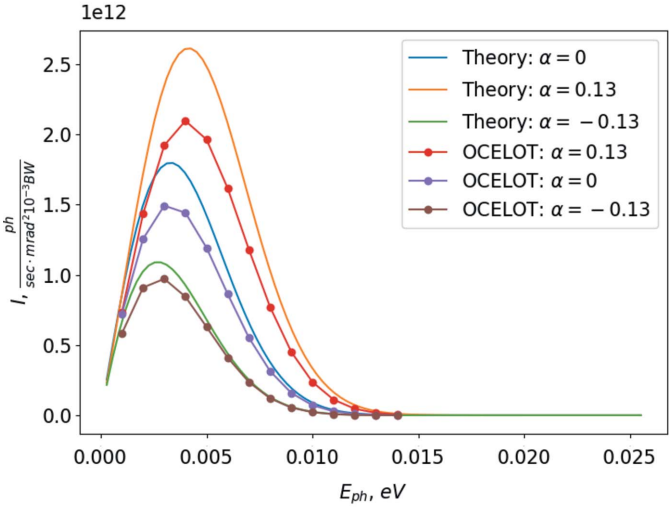

Figure 8
Maximum intensity as a function of the fundamental tune for different chirps. In the numerical calculations the undulator end-poles are characterized by one-quarter of the on-axis magnetic field from the other poles.

$$\bar{f}_\tau(\omega) = \frac{1}{N_e}\left\langle \sum_{j=1}^{N_e} \exp(i\omega\tau_j) \right\rangle, \tag{30}$$

and therefore

$$\bar{f}_\tau[\omega\chi(z')] = \frac{1}{N_e}\left\langle \sum_{j=1}^{N_e} \exp\left[i\omega\chi(z')\,\tau_j\right] \right\rangle. \tag{31}$$

Then, with the help of equation (31), equation (28) gives

$$\begin{aligned}\left\langle I(z,\theta,\omega)\right\rangle = \frac{cz^2}{2\pi}\left\langle \left|\widetilde{E}\right|^2 \right\rangle = \frac{cz^2}{2\pi}|A|^2 \\ \times \int_{-L_u/2}^{L_u/2} dz' \int_{-L_u/2}^{L_u/2} dz'' B(z')\,B^*(z'') \\ \times \left\langle \sum_{m,n=1}^{N_e} \exp\left[i\omega\chi(z')\,\tau_m - i\omega\chi(z'')\,\tau_n\right] \right\rangle. \end{aligned} \tag{32}$$

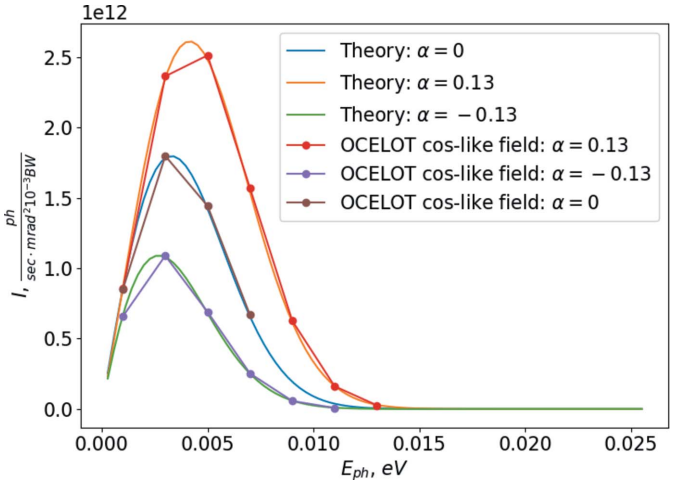

Figure 9
Maximum intensity as a function of the fundamental tune for different chirps. In the numerical calculations, a cos-like magnetic field profile was chosen.

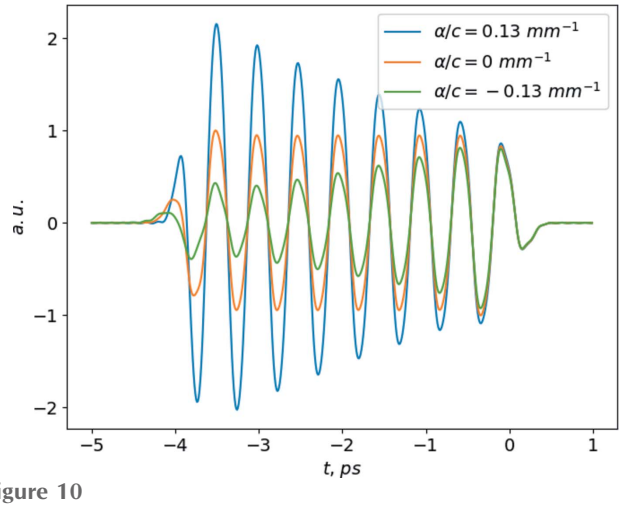

Figure 10
Coherent part of the on-axis field obtained by synthesizing, from the results in this section, photon energies between 0.1 meV and 30 meV. Orange, blue and green lines refer to different electron energy chirp conditions.

Clearly

$$\left\langle \sum_{m,n=1}^{N_e} \exp\left[i\omega\chi(z')\tau_m - i\omega\chi(z'')\tau_n\right]\right\rangle = \left\langle \sum_{j=1}^{N_e} \exp\left\{i\omega[\chi(z') - \chi(z'')]\tau_j\right\} + \sum_{m\neq n}^{N_e} \exp\left[i\omega\chi(z')\tau_m - i\omega\chi(z'')\tau_n\right]\right\rangle = N_e \bar{f}_\tau[\omega\chi(z') - \omega\chi(z'')] + N_e(N_e - 1)\bar{f}_\tau[\omega\chi(z')]\bar{f}^*[\omega\chi(z'')]. \quad (33)$$

Note that the argument of $\bar{f}_\tau$ in the first term is not zero, as it usually is in calculations of the incoherent summation of phasors. The reason is that we grouped the full dependence on the arrival time of the jth particle in the phasors that we

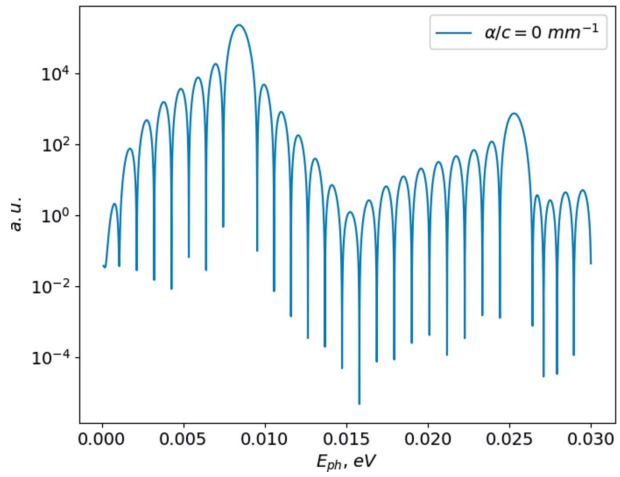

Figure 11
On-axis spectrum corresponding to $\alpha/c = 0$ (orange line in Fig. 10).

subsequently summed up. Given the fact that the electron distribution has a chirp, it follows that the phasors depend on $\chi(z)$, which leads to a non-zero argument in the first term. Substituting into equation (32) we have

$$\langle I(z,\theta,\omega)\rangle = \frac{cz^2}{2\pi}\left\langle\left|\tilde{E}\right|^2\right\rangle = \frac{cz^2}{2\pi}|A|^2\int_{-L_u/2}^{L_u/2}\mathrm{d}z'\int_{-L_u/2}^{L_u/2}\mathrm{d}z'' \times B(z')\,B^*(z'')\Big\{N_e\bar{f}_\tau[\omega\chi(z') - \omega\chi(z'')] + N_e(N_e-1)\bar{f}_\tau[\omega\chi(z')]\bar{f}_\tau^*[\omega\chi(z'')]\Big\}. \quad (34)$$

Finally, we substitute equations (25), (26) and (27) back into equation (37),

$$\langle I(z,\theta,\omega)\rangle = \frac{cz^2}{2\pi}\left\langle\left|\tilde{E}\right|^2\right\rangle = \frac{cz^2}{2\pi}\frac{K^2\omega^2e^2A_{JJ}^2}{4c^4\gamma_0^2z^2}\int_{-L_u/2}^{L_u/2}\mathrm{d}'z\int_{-L_u/2}^{L_u/2}\mathrm{d}''z \times \exp\left[i\left(\frac{\omega\theta^2}{2c} + \frac{\omega-\omega_1}{\omega_1}k_u\right)(z'-z'')\right] \times \left\{N_e\bar{f}_\tau\left[\omega\left(\frac{1+K^2/2}{c\gamma_0^3}\alpha(z''-z')\right)\right] + N_e(N_e-1)\bar{f}_\tau\left[\omega\left(1-\frac{1+K^2/2}{c\gamma_0^3}\alpha(z'+L_u/2)\right)\right] \times \bar{f}_\tau^*\left[\omega\left(1-\frac{1+K^2/2}{c\gamma_0^3}\alpha(z''+L_u/2)\right)\right]\right\}, \quad (35)$$

and we obtain a generalization of the usual formula for coherent and incoherent emission,

$$\begin{aligned}\langle I(z,\theta,\omega)\rangle &= \frac{cz^2}{2\pi}\left\langle\left|\widetilde{E}\right|^2\right\rangle \\ &= N_{\rm e}\frac{K^2\omega^2e^2A_{JJ}^2}{8\pi c^3\gamma_0^2}\int_{-L_{\rm u}/2}^{L_{\rm u}/2}{\rm d}'z\int_{-L_{\rm u}/2}^{L_{\rm u}/2}{\rm d}''z \\ &\times\exp\left[i\left(\frac{\omega\theta^2}{2c}+\frac{\omega-\omega_1}{\omega_1}k_{\rm u}\right)(z'-z'')\right] \\ &\times\bar{f}_\tau\left[\omega\left(\frac{1+K^2/2}{c\gamma_0^3}\alpha(z''-z')\right)\right] \\ &+ N_{\rm e}(N_{\rm e}-1)\frac{K^2\omega^2e^2A_{JJ}^2}{8\pi c^3\gamma_0^2} \\ &\times\left|\int_{-L_{\rm u}/2}^{L_{\rm u}/2}{\rm d}'z\exp\left[i\left(\frac{\omega\theta^2}{2c}+\frac{\omega-\omega_1}{\omega_1}k_{\rm u}\right)z'\right]\right. \\ &\times\left.\bar{f}_\tau\left[\omega\left(1-\frac{1+K^2/2}{c\gamma_0^3}\alpha(z'+L_{\rm u}/2)\right)\right]\right|^2. \end{aligned} \tag{36}$$

Note the non-intuitive expression for the incoherent part of the radiation, that is the first term in equation (36), which follows from the fact that the argument of $\bar{f}_\tau$ in the first term of equation (33) is not zero. We now verify that this incoherent term can be written in the usual intuitive way, as the integral of single-particle intensities averaged over the electron energy distribution. In fact, remembering that the power from the kth electron is

$$\begin{aligned}I_k(z,\theta,\omega) &= \frac{K^2\omega^2e^2A_{JJ}^2}{8\pi c^3\gamma_k^2} \\ &\times\left|\int_{-L_{\rm u}/2}^{L_{\rm u}/2}{\rm d}'z\exp\left[i\left(\frac{\omega\theta^2}{2c}+\frac{\omega-\omega_{1k}}{\omega_{1k}}k_{\rm u}\right)z'\right]\right|^2\end{aligned} \tag{37}$$

and that

$$N_{\rm e}\bar{f}_\tau[\omega\chi(z')-\omega\chi(z'')]=\left\langle\sum_{k=1}^{N_{\rm e}}\exp\{i\omega[\chi(z')-\chi(z'')]\tau_k\}\right\rangle, \tag{38}$$

we see that the first term in equation (36) can simply be written [upon substitution of equation (38)] as

$$\begin{aligned}\langle I_{\rm inc}(z,\theta,\omega)\rangle &= \frac{K^2\omega^2e^2A_{JJ}^2}{8\pi c^3\gamma_0^2}\left\langle\sum_{k=1}^{N_{\rm e}}\left|\int_{-L_{\rm u}/2}^{L_{\rm u}/2}{\rm d}'z\right.\right. \\ &\times\left.\left.\exp\left[i\left(\frac{\omega\theta^2}{2c}+\frac{\omega-\omega_1}{\omega_1}k_{\rm u}\right)z'+i\omega\chi(z')\tau_k\right]\right|^2\right\rangle \\ &=\left\langle\sum_{k=1}^{N_{\rm e}}\frac{K^2\omega^2e^2A_{JJ}^2}{8\pi c^3\gamma_k^2}\right. \\ &\times\left.\left|\int_{-L_{\rm u}/2}^{L_{\rm u}/2}{\rm d}'z\exp\left[i\left(\frac{\omega\theta^2}{2c}+\frac{\omega-\omega_{1k}}{\omega_{1k}}k_{\rm u}\right)z'\right]\right|^2\right\rangle \\ &=\left\langle\sum_{k=1}^{N_{\rm e}}I_k(z,\theta,\omega)\right\rangle \\ &= N_{\rm e}\frac{K^2\omega^2e^2A_{JJ}^2}{8\pi c^3}\int_0^\infty\frac{{\rm d}\gamma}{\gamma^2}f_\gamma(\gamma) \\ &\times\left|\int_{-L_{\rm u}/2}^{L_{\rm u}/2}{\rm d}'z\exp\left[i\left(\frac{\omega\theta^2}{2c}+\frac{\omega-2k_{\rm u}c\bar{\gamma}_z^2}{2c\bar{\gamma}_z^2}\right)z'\right]\right|^2,\end{aligned} \tag{39}$$

where $\bar{\gamma}_z=\gamma/(1+K^2/2)^{1/2}$, $f_\gamma(\gamma)=\int{\rm d}\tau\,{\rm d}^2\eta\,{\rm d}^2l\,f(\mathbf{l},\boldsymbol{\eta},\gamma,\tau)$, having used equation (7). This is just equation (21), where we approximated $\gamma\simeq\gamma_0$ in the factor $1/\gamma^2$ under the integral sign.

APPENDIX *B*
Discussion of dynamical effects from a chirped beam in the case of generic motion

In general, the slowly varying envelope of the Fourier transform of the electric field of a moving charge in the paraxial approximation is given by [for a treatment keeping similar notations, see Geloni *et al.* (2007) for example]

$$\begin{aligned}\widetilde{\mathbf{E}}(z,\mathbf{r}_\perp,\omega) = &-\frac{i\omega e}{c^2}\int_{-\infty}^{\infty}{\rm d}'z\frac{1}{z-z'}\left[\frac{\mathbf{v}(\mathbf{z}')}{c}-\frac{\mathbf{r}_\perp-\mathbf{r}'_\perp(z')}{z-z'}\right] \\ &\times\exp\left\{i\omega\left[\frac{|\,\mathbf{r}_\perp(z')-\mathbf{r}'_\perp\,|^2}{2c(z-z')}+\left(\frac{s(z')}{v}-\frac{z'}{c}\right)\right]\right\}.\end{aligned} \tag{40}$$

Here $s(z')$ is the curvilinear abscissa along the particle trajectory, the integration is assumed to extend along the entire trajectory, the observer is assumed located downstream of the source, and

$$\omega\left[\frac{s(z_2)-s(z_1)}{v}-\frac{z_2-z_1}{c}\right]=\int_{z_1}^{z_2}{\rm d}\bar{z}\,\frac{\omega}{2\gamma_z^2(\bar{z})c}. \tag{41}$$

Still in full generality, assuming the reference trajectory to be as that for $\tau_k=0$ we see that (assuming $v\simeq c$)

$$
\begin{aligned}
x(z') &= x_0(z') + R_{16}(z')\frac{\Delta\gamma}{\gamma_0},\\
v_x(z') &= v_{0x}(z') + cR_{26}(z')\frac{\Delta\gamma}{\gamma_0},\\
y(z') &= y_0(z') + R_{36}(z')\frac{\Delta\gamma}{\gamma_0},\\
v_y(z') &= v_{0y}(z') + cR_{46}(z')\frac{\Delta\gamma}{\gamma_0},\\
s(z') &= s_0(z') + R_{56}(z')\frac{\Delta\gamma}{\gamma_0}.
\end{aligned}
\tag{42}
$$

In general, one should substitute all of equation (42) into equation (40).

Although we refrain from doing so explicitly, one can very easily do so and work out, for instance, the case of edge radiation. For this setup, of course, the function $R_{56}(\delta z') = -\delta z'/\gamma_0^2$ should be used, instead of equation (12), and the electrons move along the longitudinal axis.

Back to the case of planar undulator radiation, one could in principle start from equation (40). The application of the resonance approximation can be enforced by neglecting terms related with the gradient of the charge density distribution [that is the term $[\mathbf{r}_\perp - \mathbf{r}'_\perp(z')]/(z-z')$ under square brackets, which includes the entire y-polarization contribution] and also the constrained particle motion in that part of the phase factor which follows from the Green's function, that is the term $\mathbf{r}_\perp(z')$ in the squared modulus in the phase factor.

One can then proceed further, assuming that the R_{26} term is small, which is the case for $\alpha\sigma_\tau \ll \gamma_0$, and that the kth electron arrives at time τ_k, while the reference arrives at time $t = 0$ at the entrance of the undulator. Then, the kth electron accumulates delay (or makes up for it) as it moves inside the undulator, according to $R_{56}(\delta z')\Delta\gamma/\gamma_0$, where $\delta z'$ is the distance travelled inside of the undulator. If $z' = 0$ indicates the middle of the undulator, then $\delta z' = z' + L_\mathrm{u}/2$ and the field from the kth electron is therefore given by

$$
\begin{aligned}
\widetilde{E}_k(z, \mathbf{r}_\perp, \omega) \simeq\ & -\frac{i\omega e}{c^2}\int_{-L_\mathrm{u}/2}^{L_\mathrm{u}/2} \mathrm{d}'z\,\frac{1}{z-z'}\frac{\mathbf{v}(z')}{c}\\
& \times \exp\left\{i\omega\left[\frac{r_\perp^2}{2c(z-z')} + \left(\frac{s_0(z')}{v} - \frac{z'}{c}\right)\right]\right\}\\
& \times \exp\left[i\omega R_{56}(z' + L_\mathrm{u}/2)\,\frac{\alpha\tau_k}{\gamma_0} + i\omega\tau_k\right].
\end{aligned}
\tag{43}
$$

Not surprisingly, the phase factor in the second line is the same as in the kth term of equation (20), second line.

Acknowledgements

We thank Michael Gensch, Bertram Green and Sergey Kovalev (HZDR) for fruitful discussions and for allowing us, as copyright holders, to reproduce Fig. 1. We thank Bart Faatz, Evgeni Saldin and Nikola Stojanovich (DESY) for useful discussions and their interest in this work.

References

Ackermann, W., Asova, G., Ayvazyan, V., Azima, A., Baboi, N., Bähr, J., Balandin, V., Beutner, B., Brandt, A. & Bolzmann, A. (2007). *Nat. Photon.* **1**, 336–342.

Agapov, I., Geloni, G., Tomin, S. & Zagorodnov, I. (2014). *Nucl. Instrum. Methods Phys. Res. A*, **768**, 151–156.

DESY S2E Simulations (2013). *FLASH I, 500 pC*, http://www.desy.de/fel-beam/s2e/flash/Nominal/flashI/nom500pC.html.

FLASH (2018). *FLASH*, https://flash.desy.de.

Geloni, G., Saldin, E., Schneidmiller, E. & Yurkov, M. (2007). *Opt. Commun.* **276**, 167–179.

Gensch, M., Bittner, L., Chesnov, A., Delsim-Hashemi, H., Drescher, M., Faatz, B., Feldhaus, J., Fruehling, U., Geloni, G. A., Gerth, Ch., Grimm, O., Hahn, U., Hesse, M., Kapitzki, S., Kocharyan, V., Kozlov, O., Matyushevsky, E., Morozov, N., Petrov, D., Ploenjes, E., Roehling, M., Rossbach, J., Saldin, E. L., Schmidt, B., Schmueser, P., Schneidmiller, E. A., Syresin, E., Willner, A. & Yurkov, M. V. (2008). *Infrared Phys. Technol.* **51**, 423–425.

Green, B., Kovalev, S., Asgekar, V., Geloni, G., Lehnert, U., Golz, T., Kuntzsch, M., Bauer, C., Hauser, J., Voigtlaender, J., Wustmann, B., Koesterke, I., Schwarz, M., Freitag, M., Arnold, A., Teichert, J., Justus, M., Seidel, W., Ilgner, C., Awari, N., Nicoletti, D., Kaiser, S., Laplace, Y., Rajasekaran, S., Zhang, L., Winnerl, S., Schneider, H., Schay, G., Lorincz, I., Rauscher, A. A., Radu, I., Mährlein, S., Kim, T. H., Lee, J. S., Kampfrath, T., Wall, S., Heberle, J., Malnasi-Csizmadia, A., Steiger, A., Müller, A. S., Helm, M., Schramm, U., Cowan, T., Michel, P., Cavalleri, A., Fisher, A. S., Stojanovic, N. & Gensch, M. (2016). *Sci. Rep.* **6**, 22256.

Nodvick, J. S. & Saxon, D. S. (1954). *Phys. Rev.* **96**, 180–184.

Onuki, H. & Elleaume, P. (2003). *Undulators, Wigglers and their Applications*, p. 438. London: Taylor & Francis (2003)

Tanaka, T. & Kitamura, H. (2001). *J. Synchrotron Rad.* **8**, 1221–1228.

Tanikawa, T., Karabekyan, S., Kovalev, S., Casalbuoni, S., Asgekar, V., Gensch, M. & Geloni, G. (2018). *Superradiant Undulator Radiation for Selective THz Control Experiments at XFELs*, European XFEL Report. European XFEL, Hamburg, Germany.

Williams, G. P. (2004). *Philos. Trans. R. Soc. London. Ser. A*, **362**, 403–414.

Zagorodnov, I. & Dohlus, M. (2011). *Phys. Rev. ST Accel. Beams*, **14**, 014403.

Zagorodnov, I., Feng, G. & Limberg, T. (2016). *Nucl. Instrum. Methods Phys. Res. A*, **837**, 69–79.